Structural Basis for the Anisotropic Thermal Expansion of Aluminum Titanate, Al_2TiO_5, at Elevated Temperatures

Alexandra Doncieux*, Keisuke Ninomiya, Nobuo Ishizawa, Toshitaka Ota and Marc Huger*

Advanced Ceramics Research Center, Nagoya Institute of Technology,
10-6-29, Asahigaoka, Tajimi, Gifu 507-0071, JAPAN

*ENSCI, Centre Européen de la Céramique, 12, rue Atlantis,
87068 Limoges Cedex, FRANCE

Evolution of the undoped and Mg-doped Al_2TiO_5 crystal structures at elevated temperatures up to ~1300 K was investigated by the single-crystal X-ray diffraction technique. The compounds crystallize in the pseudobrookite-type $^{[4c]}M1^{[8f]}M2_2O_5$ structure with the space group *Cmcm*, containing crystallographically independent M1 site at the Wyckoff position of 4*c* and M2 site at 8*f* for the metal atoms. The structural formula was found to be $^{[4c]}[Al_{0.615(3)}Ti_{0.385(3)}]^{[8f]}[Al_{0.693(2)}Ti_{0.307(2)}]_2O_5$ for the undoped Al_2TiO_5 and $^{[4c]}[Al_{0.616(9)}Ti_{0.384(9)}]^{[8f]}[Al_{0.562(4)}Ti_{0.373(4)}Mg_{0.065(10)}]_2O_5$ for the Mg-doped one from the population analysis of the metal atoms. The mean thermal expansion coefficients were approximately -3.8×10^{-6} along the a-axis, 11.0×10^{-6} along the b-axis and 20.0×10^{-6} along the c-axis. During heating, the tunnels running along the c-axis in the structure change shape gradually with a characteristic buckling deformation of the chevron-shaped pillars composed of metal-oxygen bonds, resulting in an expansion of the tunnel along all directions perpendicular to the a-axis and the associated Poisson contraction along the a-axis. The large anisotropy in thermal expansion of the compounds, especially the negative thermal expansion along the a-axis, was thus explained from atomistic point of view.

Keywords: Al_2TiO_5, Mg-doped Al_2TiO_5, high-temperature structures, anisotropic thermal expansion, Poisson deformation

1. Introduction

Crystals of aluminum titanate (tieilite) Al_2TiO_5 adopt an Fe_2TiO_5 pseudobrookite-type structure [1, 2]. Sintered ceramics of Al_2TiO_5 and related ones are known to exhibit a low thermal expansion, which is an important property for the thermal shock resistant materials for the industrial applications [3–7]. The relationship between the macroscopic thermal expansion behaviour and the microscopic evolution of atomic arrangement in the structure, however, has not been well clarified since the pioneering work by Morosin and Lynch in 1972 [8]. The present study thus aims to afford structural information at elevated temperatures through the in-situ single-crystal X-ray diffraction experiments in order to establish the structural basis for the anisotropic thermal expansion in Al_2TiO_5. The Al_2TiO_5 ceramics are usually synthesized with cation dopants such as Mg, since the pure compound possesses a eutectoid decomposition temperature around 1553 K [3, 9], and is thermodynamically unstable at room temperature. The present study, therefore, also involves the high-temperature experiments on the Mg-doped Al_2TiO_5 and discusses the effect of Mg-doping on the structural evolution.

2. Experimental

The undoped Al_2TiO_5 sintered sample (AT) was synthesized by pressing the spray-drying ceramic powders (TM-20P, Marusu Co., Ltd.) in a mold and then sintering the material at 1873−1923 K for 16 h. The Mg-doped Al_2TiO_5 sintered sample (ATM) was prepared by the coauthors' group in France [10], by sintering a mixture of Al_2O_3, TiO_2 and MgO powders in a molar ratio of 0.406:0.525:0.069 at 1873 K for 2 h. The molar ratio corresponds to 85.5 mol% Al_2TiO_5 + 14.5 mol% $MgTi_2O_5$. Compositions of crystals were analyzed by the electron backscattering diffraction (EBSD) technique using JSM-7001FF scanning electron microscope (JEOL, Co., Ltd.). Chemical impurities of Si, Fe and Ca were detected in both samples but their amounts were negligibly small for the quantitative analysis. Determination of the Mg content in ATM is detailed in **Section 3.2**.

Diffraction experiments were carried out using a single-crystal X-ray diffraction apparatus (Mo Kα) with a two-dimensional charge-coupled device detector (Bruker Smart Apex II). The temperature of the crystal was controlled in a hot nitrogen gas stream using a crystal heater attached to the diffractometer. The sample

Table 1. Summary of structure refinements of the undoped Al_2TiO_5 (sample ATh_11).

Temperature (K)	322	631	943	1254
a (Å)	3.59020(10)	3.58590(10)	3.58260(10)	3.57990(10)
b (Å)	9.4367(2)	9.4649(2)	9.4981(2)	9.5366(2)
c (Å)	9.6540(2)	9.7085(2)	9.7710(2)	9.8404(2)
V (Å^3)	327.074(13)	329.508(13)	332.487(13)	335.952(14)
Space group	*Cmcm*	*Cmcm*	*Cmcm*	*Cmcm*
Number of reflections measured	8616	8762	8855	8972
θ_{max}	50.57	50.59	50.58	50.57
R_{int}	0.0531	0.0539	0.0557	0.0575
Number of independent reflections	996	1002	1013	1023
Number of reflections with I > 3σ(I)	819	780	729	651
R (I > 3σ(I))	0.026	0.0278	0.0324	0.033
R_w (I > 3σ(I))	0.0328	0.0364	0.0408	0.0424
Goodness of fit	1.61	1.68	1.81	1.8
M1 at 4*c* (0, *y*, 1/4)				
y	0.18501(3)	0.18372(4)	0.18221(5)	0.18063(5)
Ueq	0.00728(7)	0.01414(8)	0.01893(10)	0.02513(12)
pop(Al)	0.612(3)	0.613(3)	0.614(4)	0.619(4)
*U*11	0.00674(12)	0.01366(14)	0.01821(17)	0.0240(2)
*U*22	0.00833(13)	0.01523(15)	0.02029(18)	0.0267(2)
*U*33	0.00676(11)	0.01354(13)	0.01829(16)	0.02477(19)
M2 at 8*f* (0, *y*, *z*)				
y	0.13496(3)	0.13472(3)	0.13459(4)	0.13453(4)
z	0.56159(3)	0.56165(3)	0.56164(4)	0.56181(4)
Ueq	0.00817(5)	0.01522(6)	0.02024(8)	0.02658(9)
pop(Al)	0.6942(16)	0.6937(17)	0.693(2)	0.6903(19)
*U*11	0.00637(9)	0.01301(11)	0.01704(13)	0.02193(15)
*U*22	0.00891(10)	0.01543(11)	0.02015(14)	0.02587(16)
*U*33	0.00925(9)	0.01720(12)	0.02354(14)	0.03193(17)
*U*23	0.00027(6)	0.00032(7)	0.00041(10)	0.00048(11)
O1 at 4*c* (0, *y*, 1/4)				
y	0.75720(11)	0.75635(13)	0.75553(16)	0.75457(18)
*U*eq	0.00859(17)	0.0166(2)	0.0230(3)	0.0307(4)
*U*11	0.0073(3)	0.0145(4)	0.0190(5)	0.0248(6)
*U*22	0.0093(3)	0.0177(4)	0.0255(5)	0.0322(7)
*U*33	0.0092(3)	0.0177(4)	0.0243(5)	0.0350(7)
O2 at 8*f* (0, *y*, *z*)				
y	0.04844(7)	0.04824(9)	0.04789(11)	0.04756(12)
z	0.11658(7)	0.11651(9)	0.11634(10)	0.11639(12)
*U*eq	0.00924(13)	0.01786(17)	0.0246(2)	0.0326(3)
*U*11	0.0132(3)	0.0257(4)	0.0362(5)	0.0478(7)
*U*22	0.0073(2)	0.0139(3)	0.0183(3)	0.0239(4)
*U*33	0.00726(19)	0.0140(2)	0.0194(3)	0.0259(4)
*U*23	−0.00091(16)	−0.0016(2)	−0.0018(3)	−0.0025(3)
O3 at 8*f* (0, *y*, *z*)				
y	0.31227(7)	0.31224(9)	0.31203(11)	0.31176(13)
z	0.07195(8)	0.07203(10)	0.07236(12)	0.07238(14)
*U*eq	0.00936(13)	0.01754(16)	0.0245(2)	0.0323(3)
*U*11	0.0068(2)	0.0134(3)	0.0176(3)	0.0226(4)
*U*22	0.0086(2)	0.0164(3)	0.0231(4)	0.0302(5)
*U*33	0.0127(2)	0.0228(3)	0.0326(4)	0.0442(6)
*U*23	0.00116(18)	0.0025(2)	0.0036(3)	0.0049(4)

temperature was calibrated using a cubic polynomial.

A rectangular fragment (sample name: ATh_11) was chosen from AT and used for the high-temperature experiments. The fragment was surrounded by six well-developed faces; (0 0 ±1), (0 ±1 0) and (±1 0 0) in terms of the orthorhombic *Cmcm* lattice, with the longest edge of ~250 μm along the a-axis. Unit cell dimensions were measured at 10 different temperatures between 322 and 1254 K during heating and cooling processes, respectively. Intensity data collections for structure

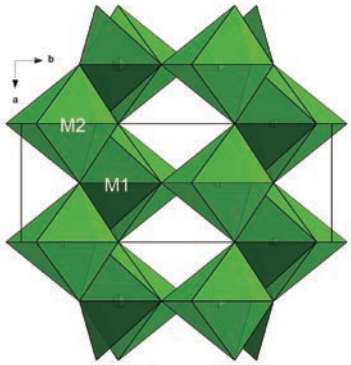

Figure 1. Octahedral drawing of the pseudobrookite-type $M1_1M2_2O_5$ structure viewed along the c-axis.

determination were then carried out at 322, 631, 943 and 1254 K in the 2θ range up to 100°, taking approximately 9 h at each temperature.

Similar diffraction experiments were carried out for ATM. A fragment was chosen from the ATM sintered sample and ground into a sphere of approximately 90 μm in diameter (sample name: ATMh_19). The high-temperature experiments were executed at 296, 373, 580, 787, 995 and 1254 K during heating, and 995, 787, 580, 373 and 296 K during cooling, in this sequence. After this first run, the second run was executed at 296, 631, 995 and 1306 K during heating, and at 631 (1st), 631 (2nd), 373 (1st), 373 (2nd) and 296 K during cooling. These heating and cooling processes in the two runs were named as heat 1, cool 1, heat 2 and cool 2, respectively. The two runs and the doubled experiments at 631 and 373 K in the cooling process of the second run were necessary to examine the hysteresis of the thermal expansion behavior of the a-axis in ATM, as described in **Section 3.3**. Structure determination of the ATMh_19 sample was also carried out at each temperature, but most experiments were done in a rapid way within 3 h in the range 2θ < 60° for the primary purpose of the determination of unit cell dimensions. Therefore, the data qualities of ATMh_19 were slightly inferior to those of ATh_11.

All the frame data were processed by SAINT [11]. The absorption correction was carried out using SADABS [12]. Structures were solved by SUPERFLIP [13] and refined by Jana2006 [14]. Structures were visualized by DIAMOND [15] and VESTA [16]. Full structure data about ATh_11 and ATMh_19 are available as supplementary information in the format of the crystallographic information file (CIF).

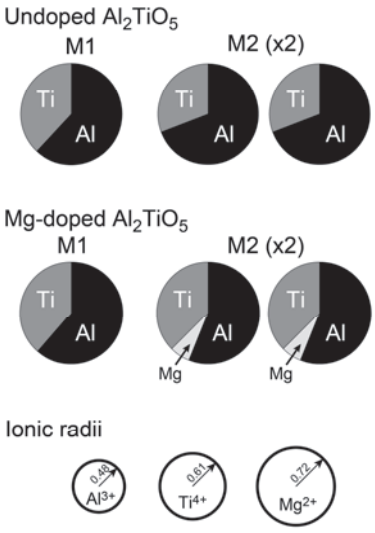

Figure 2. Distribution of metal atoms at the M1 (4*c*) and M2 (8*f*) sites in the undoped Al_2TiO_5 at 322 K and Mg-doped Al_2TiO_5 at RT. Two pie charts are drawn for M2 in accord with the ratio in number of the M1 and M2 sites. The ionic radii of Al^{3+}, Ti^{4+} and Mg^{2+} in six-ford coordination with oxygens are shown at the bottom.

3. Results and discussion

3.1 Refinements of X-ray diffraction data

The structure of pseudobrookite-type M_3O_5 has two crystallographically independent metal atom sites, M1 and M2, which are located, respectively, at the 4*c* and 8*f* Wyckoff positions of the space group *Cmcm*. Conventionally, the metal atoms are described to be surrounded by six oxygens forming rather deformed octahedra, as shown in **Fig. 1**. The results of structure refinements of the sample ATh_11 at 322, 631, 943 and 1254 K during heating are summarized in **Table 1**.

3.2 Crystal chemical formula

A sample was selected from the fragments of Mg-doped Al_2TiO_5 ceramics (ATM), and its chemical composition was investigated on twelve different points/areas by the EBSD/EDS analysis.

When *x*MgO is doped to Al_2TiO_5, the compound should have a chemical formula $Al_{2-2x}Ti_{1+x}Mg_xO_5$ in order to satisfy the electrically neutral condition under the assumptions:

i) The Al, Ti, Mg and O atoms take the formal oxidation states of +3, +4, +2 and −2, respectively.

ii) The lattice is perfect, having neither interstitial atoms nor lattice vacancies.

The EBSD/EDS analysis on ATM indicated that the mole fraction of *x*MgO is 0.13(2), where the number in parentheses indicates the estimated standard uncertainty. The chemical composition of the Mg-doped Al_2TiO_5 becomes, accordingly, $Al_{1.74(4)}Ti_{1.13(2)}Mg_{0.13(2)}O_5$. The Al_2O_3:TiO_2:MgO molar ratio in this composition corresponds to 0.408:0.531:0.061, which was very close to the ratio of 0.406:0.525:0.069 of the powder mixture before sintering, as stated in **Section 2**. Since the chemical impurities were found to be negligibly small by the EDS analysis, a stoichiometric composition of Al_2TiO_5 was assumed for the undoped Al_2TiO_5 crystal (AT).

It is known that that Al^{3+}, Ti^{4+} and Mg^{2+} can occupy M1 and M2 sites in the formula $^{[4c]}M1_1{}^{[8f]}M2_2O_5$ [8]. Therefore, the general structural formula can be written as

$$^{[4c]}[Al_{a1}Ti_{t1}Mg_{m1}]_1{}^{[8f]}[Al_{a2}Ti_{t2}Mg_{m2}]_2O_5,$$

where $a1$, $t1$, $m1$ are the population variables of Al, Ti and Mg at M1, respectively, and $a2$, $t2$ and $m2$ are those at M2. Assuming that M1 and M2 sites are fully occupied:

$$a1 + t1 + m1 = 1 \quad (1)$$
$$a2 + t2 + m2 = 1 \quad (2)$$

From the comparison between the structural and chemical formulae,

$$a1 + 2\,a2 = 2 - 2x \quad (3)$$
$$t1 + 2\,t2 = 1 + x \quad (4)$$
$$m1 + 2\,m2 = x \quad (5)$$

These five equations (1)–(5), among which any four are independent, have six population variables, $a1$, $a2$, $t1$, $t2$, $m1$ and $m2$. Therefore, the structural formula can be expressed using any two variables, for example, $m2$ (the Mg population at M2) and $t2$ (the Ti population at M2), as

$$^{[4c]}[Al_{-2x+2t2+2m2}Ti_{1+x-2t2}Mg_{x-2m2}]_1{}^{[8f]}[Al_{1-t2-m2}Ti_{t2}Mg_{m2}]_2O_5.$$

Since $x = 0$, i.e., $m1 = m2 = 0$, in the undoped Al_2TiO_5, the structural formula can be written as a function of a single population variable,

$$^{[4c]}[Al_{2t2}\,Ti_{1-2t2}]_1{}^{[8f]}[Al_{1-t2}Ti_{t2}]_2O_5.$$

In the least-squares structural refinements of the Mg-doped Al_2TiO_5 (ATM), the population of Mg at M1 site (i.e. $m1$) became always slightly negative at all the temperatures. Accordingly, $m1$ was fixed at zero, and $m2$ was constrained at $x/2 = 0.065(10)$ in the further refinements. The structural formula of ATM was written as,

$$^{[4c]}[Al_{-x+2t2}\,Ti_{1+x-2t2}]_1{}^{[8f]}[Al_{1-t2-x/2}Ti_{t2}\,Mg_{x/2}]_2O_5.$$

The final structural compositions were determined by averaging the values determined at all temperatures, as

$$^{[4c]}[Al_{0.615(3)}Ti_{0.385(3)}]^{[8f]}[Al_{0.693(2)}Ti_{0.307(2)}]_2O_5$$

for the undoped Al_2TiO_5 (AT), and

$^{[4c]}[Al_{0.616(9)}Ti_{0.384(9)}]^{[8f]}[Al_{0.562(4)}Ti_{0.373(4)}Mg_{0.065(10)}]_2O_5$

for the Mg-doped Al_2TiO_5 (ATM).

The distribution of metal atoms at the M1 and M2 sites is illustrated in **Fig. 2**. An important tendency is that a relatively-large [17] and low-valent Mg^{2+} stays away from the M1 site and goes to the M2 site preferentially. The reason why the Mg dopant prefers the M2 site is discussed in **Sections 3.5** and **3.6**.

Recent single-crystal X-ray diffraction study [18] reported the structural composition of the melt-quenched Al_2TiO_5 as

$^{[4c]}[Al_{0.626(7)}Ti_{0.374(7)}]_1^{[8f]}[Al_{0.687(3)}Ti_{0.313(3)}]_2O_5$.

The populations of Al/Ti at M1 and M2 agreed with those in the present sample (AT) with excellent precisions. On the other hand, Skala et al. [9] carried out a high-temperature neutron and X-ray powder diffraction study on Al_2TiO_5 and reported the composition as

$^{[4c]}[Al_{0.588(3)}Ti_{0.412(3)}]_1^{[8f]}[Al_{0.712(4)}Ti_{0.288(3)}]_2O_5$,

which is slightly different from the results of the two single-crystal studies aforementioned.

Skala et al. [9] also reported that the Al/Ti ratio at M1 and M2 in Al_2TiO_5 changes with temperature suggesting a possible metal atom exchange over the two sites at high temperatures. Temperature dependence of the Al population at M1 and M2 in AT and ATM used in the present study is shown in **Fig. 3**. The population of Al at M1 tended to increase marginally during heating, and vice versa at M2. However, the exchange population was much smaller and less significant in the present study compared with the literature [9].

3.3 Cell dimensions

Changes in the unit cell dimensions with temperature are shown in **Fig. 4**. The data points obtained from the AT sample showed a good coincidence at each temperature, irrelevant to the heating or cooling processes. Thermal expansion of the unit cell dimensions (Å) of AT can be approximated using a second order polynomial as a function of temperature T (K);

$a = 3.5958(5) - 0.204(13)\times10^{-4}\,T + 0.64(8)\times10^{-8}\,T^2$,

$b = 9.4100(15) + 0.82(4)\times10^{-4}\,T + 1.7(2)\times10^{-8}\,T^2$,

$c = 9.6059(17) + 1.41(5)\times10^{-4}\,T + 3.8(3)\times10^{-8}\,T^2$.

Morosin & Lynch [8] reported the mean thermal expansion coefficients (MTECs) of Al_2TiO_5 as -1.4×10^{-6}, 9.8×10^{-6}, and 20.6×10^{-6} along the a-, b- and c-axes, respectively, based on their single-crystal X-ray diffraction experiments at RT and 873 K. The corresponding MTEC values in the present study, calculated from the above polynomials at 293 and 873 K, are -3.8×10^{-6}, 11.0×10^{-6}, and 20.0×10^{-6} along the a-, b- and c-axes, respectively. The agreements between these values in the two studies seem fine, considering the potential impurities and lattice defects in crystals.

The Mg-doped Al_2TiO_5 (ATM) had a slightly larger unit cell dimensions compared with AT, mainly due to the size effect of cations as shown in **Fig. 2**. In addition, a curious behavior was found in the temperature dependence in the cooling process of the first run, as shown in **Fig. 4** (a); the a-length showed significantly small values during cooling compared with those during heating. This stands in contrast against the other observations in which the heating/cooling process

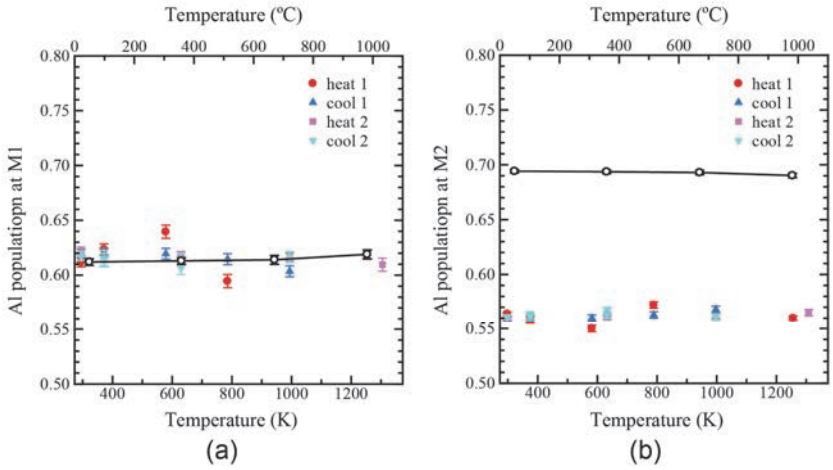

Figure 3. Aluminum population at (a) M1 and (b) M2 sites in the pseudobrookite-type $^{[4c]}M1_1^{[8f]}M2_2O_5$ structure. The open circles connected by black polyline are data obtained from the undoped Al_2TiO_5 during heating. The other scattered marks are those obtained from the Mg-doped Al_2TiO_5 during the first heating/cooling and the second heating/cooling processes. The relationship between the colour marks and processes is shown in the legend.

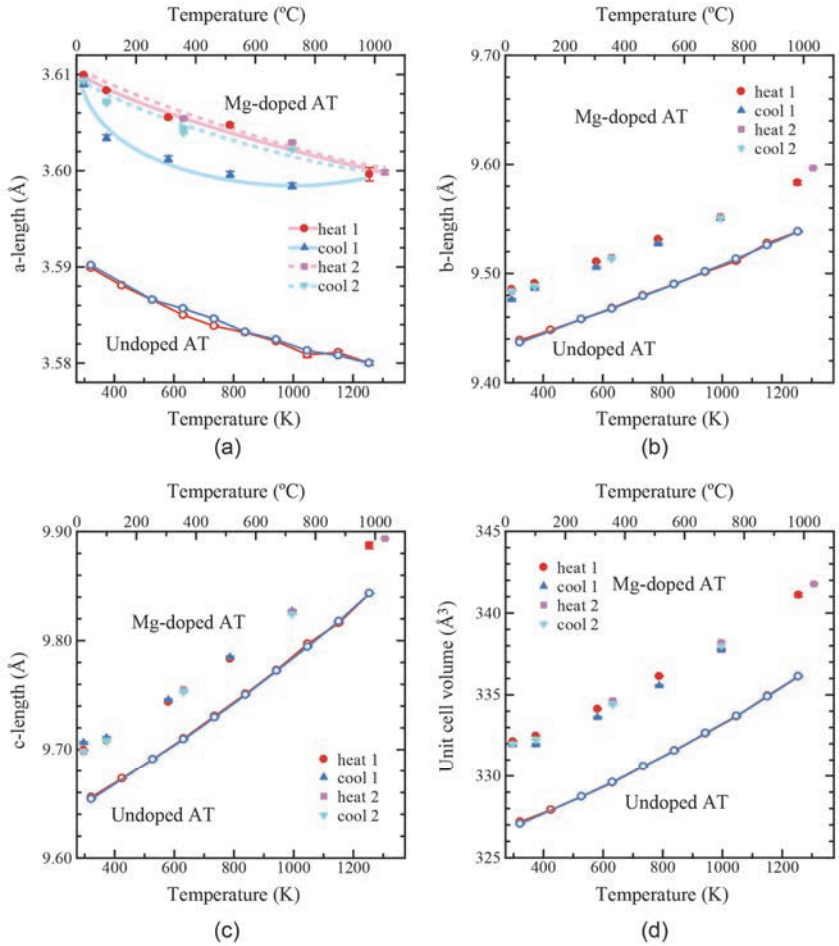

Figure 4. Changes in the unit cell dimensions with temperature; (a) a-length, (b) b-length, (c) c-length, and (d) unit cell volume. The open circles connected by polyline are data obtained from the undoped Al_2TiO_5 during heating (red) and cooling (blue). The other scattered marks are those obtained from the Mg-doped Al_2TiO_5 during the first heating/cooling and the second heating/cooling processes. The relationship between the colour marks and processes is shown in the legend.

dependency was almost undetectable. It should be noted, however, that a similar hysteresis in thermal expansion of the a-length has been observed in $MgTi_2O_5$ by the neutron powder diffraction [19] (the original unit cell vectors are converted to fit into the present study), although this phenomenon remains inexplicable.

3.4 Atomic coordinates

Changes in atomic coordinates with temperature are shown in **Fig. 5**. As listed in **Table 1**, the refinable positional parameters of the *Cmcm* pseudobrookite-type structure are limited to the *y*-coordinates of M1, M2, O1, O2 and O3 atoms and the *z*-coordinates of M2, O2 and O3 atoms. Among these parameters, the *y*-coordinates of M1 and O1 showed the most conspicuous temperature change. The directions of these changes during heating are shown in **Fig. 6** by arrows. The changes in the *y*-coordinates of M1 and O1 are closely related to the tetrahedralization of the M1 coordination polyhedron at elevated temperatures, as detailed in **Sections 3.5** and **3.6**.

3.5 M–O Distances

Changes in the M–O interatomic distances with temperature are shown in **Fig. 7**. The metal atoms at the M1 and M2 sites are surrounded by six oxygens with four short (1.8~1.9 Å) and two long (~2.1 Å) M–O distances. The most conspicuous temperature change in the M1–O distance is that the longer two M1–O bonds become much longer at elevated temperatures whereas the four short M1–O bonds stay at almost the same lengths throughout the temperature range between RT and ~1300 K. This suggests a gradual decrease in oxygen coordination number of M1 from six toward four at elevated temperatures. The displacement arrows of M1 and O1 atoms during heating, as shown in **Fig. 6**, also indicate a tendency of tetrahedralization ($M1O1_2O2_2$) during heating. It is noted that the decrease

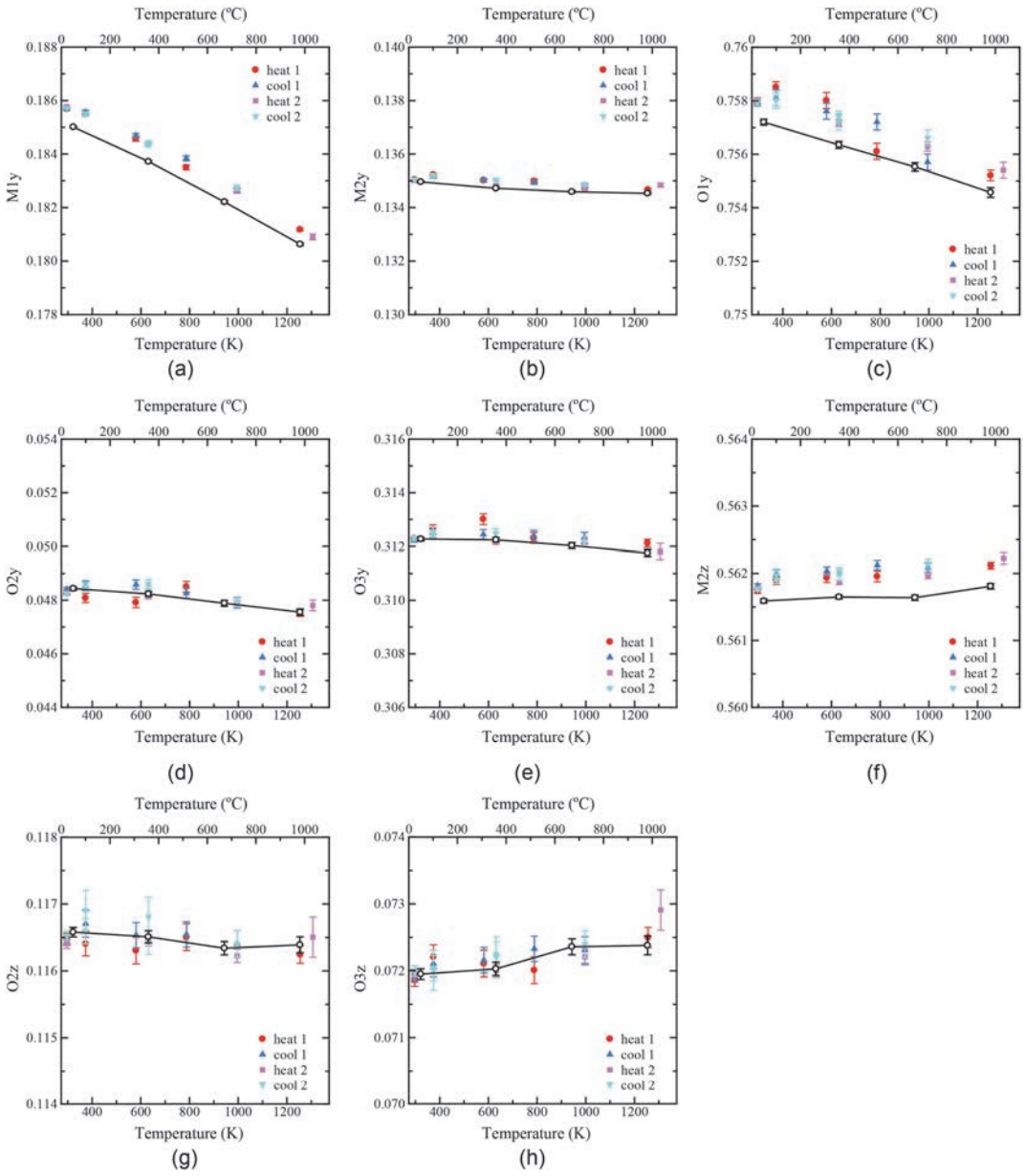

Figure 5. Temperature changes in the *y*-coordinates of (a) M1 (M1y), (b) M2 (M2y), (c) O1 (O1y), (d) O2 (O2y) and (e) O3 (O3y), and the *z*-coordinates of (f) M2 (M2z), (g) O2 (O2z) and (h) O3 (O3z). The open circles connected by polyline are data obtained from the undoped Al_2TiO_5 during heating. The other scattered marks are those obtained from the Mg-doped Al_2TiO_5 during the first heating/cooling and the second heating/cooling processes. The relationship between the colour marks and processes is shown in the legend.

in coordination number of M1 in pseudobrookite-type structure is actually evidenced in $MgTi_2O_5$ at ~1623 K [19]. A rapid increase in the two long M-O bonds is also observed for M2. However, it is noted that one M2–O2 short bond (~1.9 Å) also shows an increasing tendency during heating similar to the two long M2–O bonds, which is slightly different from the case for M1.

The tetrahedral drawing of the pseudobrookite-type structure is illustrated in **Fig. 8**, where the long M1–O and M2–O bonds (> 2 Å; dashed lines in **Fig. 6**) are neglected. Note that a pair of M2 atoms forms the edge-sharing tetrahedra with a very short M2–M2 interatomic distance of ~2.8 Å, as indicated by the yellow line. The presence of such short M2–M2 distance is the reason why the low-valent Mg^{2+} compared with Al^{3+} and Ti^{4+} prefers M2 in ATM with the formula,

$^{[4c]}[Al_{0.616(9)}Ti_{0.384(9)}]\ ^{[8f]}[Al_{0.562(4)}Ti_{0.373(4)}Mg_{0.065(10)}]_2O_5$,

to reduce the electrostatic repulsion between the M2 pair at the 8*f* sites. This short M2–M2 interatomic distance also plays an important role in the thermal expansion of the compound, which is discussed in **Section 3.7**.

Finally, it should be stressed that no strange thing happened such that any M–O bonds became shorter at elevated temperatures. All the M–O bonds are elongated during heating though the degrees of elongation are different with each other. This is of course a natural

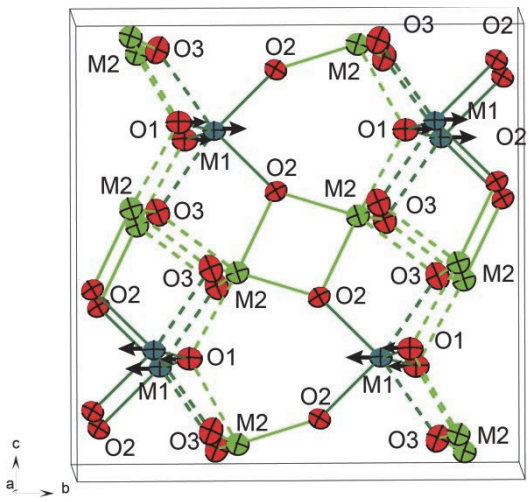

Figure 6. The room-temperature structure of the pseudobrookite-type $M1_1M2_2O_5$ (Al_2TiO_5) projected along a direction close to the a-axis. The thermal ellipsoids are drawn at 90% probability level. The shorter (≤ 2 Å) and longer (> 2 Å) M–O bonds are drawn by solid and dashed lines, respectively. The arrows attached to M1 and O1 indicate the direction of displacements of these atoms during heating.

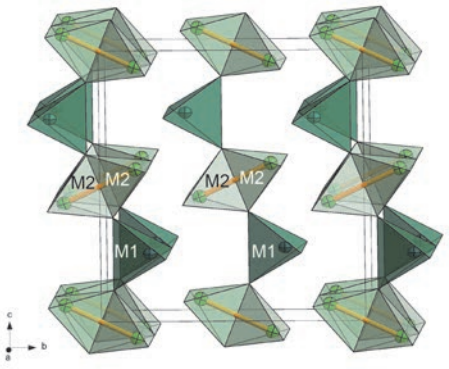

Figure 8. Tetrahedral drawing of the pseudobrookite-type structure, neglecting two long M–O bonds (dashed lines in **Fig. 6**) from the MO_6 octahedra. The very short M2–M2 interatomic distance of ~2.8 Å between the edge-sharing $M2O_4$ tetrahedra is shown by the yellow line.

tendency in most crystals, but it could be rather surprising if we recall once again that the length of the a-axis of this compound becomes short (!) at elevated temperatures. This can be explained from the Poisson effect on the tunnel deformation in the structure, which is detailed in **Section 3.8**.

3.6 Comparison of MO_6 octahedra

Four geometrical indices, the mean M–O interatomic distance (MD) in Å, the octahedral volume (OV) in $Å^3$, the quadratic elongation (QE) with no dimension, and the angle variance (AV) in square degree, are taken into consideration for comparison. The latter two indices are defined by Robinson et al. [20]: the quadratic elongation

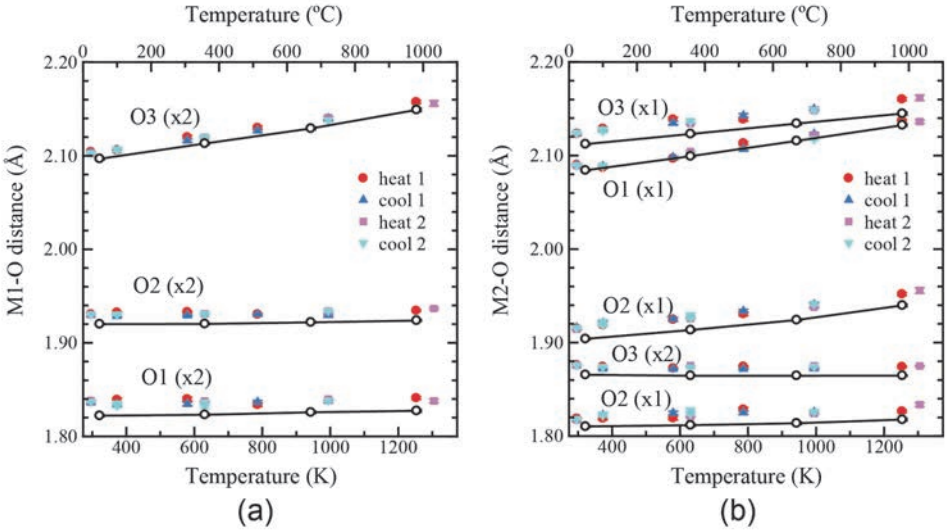

Figure 7. Temperature changes in the (a) M1–O and (b) the M2–O interatomic distances. The open circles connected by polyline are data obtained from the undoped Al_2TiO_5 during heating. The other scattered marks are those obtained from the Mg-doped Al_2TiO_5 during the first heating/cooling and the second heating/cooling processes. The relationship between the colour marks and processes is shown in the legend.

(QE) is a measure to evaluate the distribution of M–O distances (if all bonds have the same length, then QE = 1), the angle variance (AV) is a measure to evaluate the distribution of O–M–O angles (if all angles are the same, then AV = 0). Temperature changes in these four indices are shown in **Fig. 9**. The main differences between the $M1O_6$ and $M2O_6$ octahedra are as follows.

- The mean M1–O distance is larger than the mean M2–O while the octahedral volume of $M1O_6$ is smaller than that of $M2O_6$ in both AT and ATM. This is somewhat confusing, and should be treated carefully.
- The quadratic elongation shows that the M–O distances in $M1O_6$ octahedron are rather scattered compared with $M2O_6$ in both AT and ATM.
- The angle variance suggests that the $M1O_6$ octahedra are largely deformed compared with $M2O_6$ octahedra in both AT and ATM.

The geometrical features of the octahedral deformation are basically similar in AT and ATM.

3.7 M–M Distances

Changes in the M–M distance between the nearby M atoms with temperature are shown in **Fig. 10**. The six M–M interatomic distances from the shortest increase as a function of temperature. As mentioned already, the M2 site has a very short M2–M2 interatomic distance of ~2.8 Å, making a clear difference between the second coordination shells around M1 and M2. The presence of such short M2–M2 distance also prevents the tetrahedralization of coordination polyhedron at M2 in contrast with M1 at elevated temperatures.

3.8 Negative thermal expansion

From atomistic point of view, the anisotropic thermal expansion property of Al_2TiO_5 arises from the

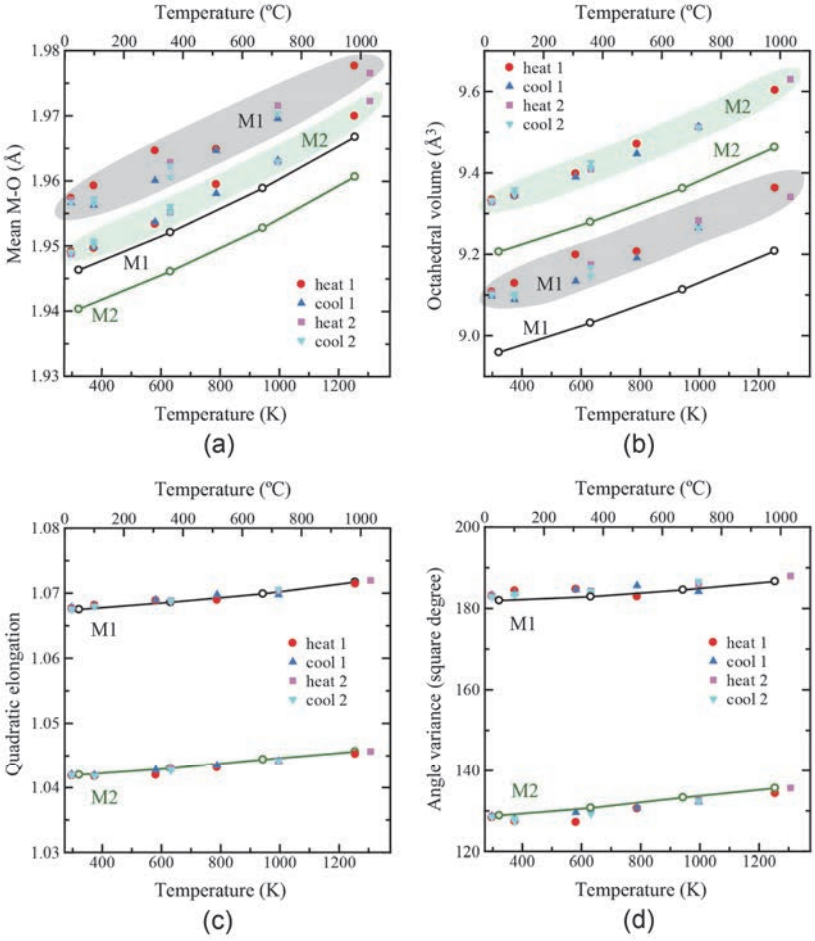

Figure 9. Temperature changes in the four geometrical indices to characterize the $M1O_6$ and $M2O_6$ octahedra; (a) mean M–O interatomic distance, (b) octahedral volume, (c) quadratic elongation, and (d) angle variance. The open circles connected by polyline are data obtained from the undoped Al_2TiO_5 during heating. The other scattered marks are those obtained from the Mg-doped Al_2TiO_5 during the first heating/cooling and the second heating/cooling processes. The relationship between the colour marks and processes is shown in the legend.

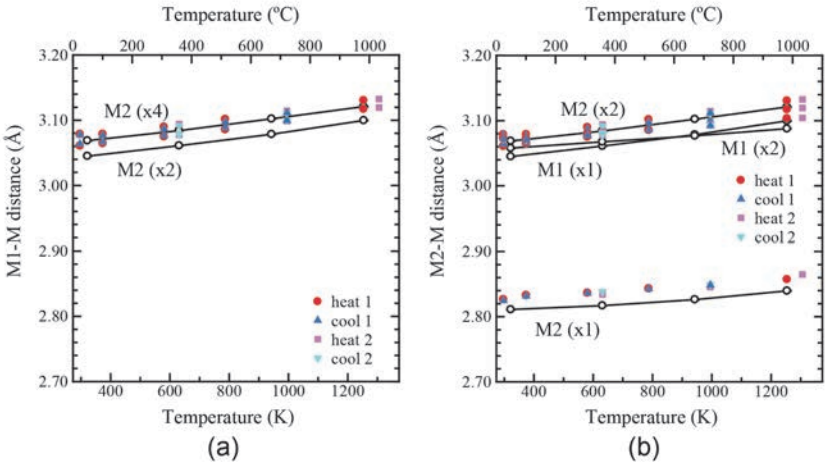

Figure 10. Temperature changes in the six M–M distances from the shortest around (a) M1 and (b) M2. The open circles connected by polyline are data obtained from the undoped Al_2TiO_5 during heating. The other scattered marks are those obtained from the Mg-doped Al_2TiO_5 during the first heating/cooling and the second heating/cooling processes. The relationship between the colour marks and processes is shown in the legend.

deformation of a tunnel-like cavity running along the c-axis, which has not been pointed out in the literature to our knowledge. As shown in **Fig. 11** (a), the tunnel has a flat ceiling and floor composed of M and O atoms at $x = \pm 1/2$, with a clearance, i.e., height of the tunnel, corresponding to the a-length. The side walls of the tunnel are composed of the M–O–M or O–M–O pillars with a chevron shape, buckling outside toward directions perpendicular to the a-axis.

The view along a direction close to the a-axis in **Fig. 11** (b) indicates that the two types of cages alternate in the tunnel along the c-axis; i) irregularly shaped cage located around $0 < z < 1/2$ and walled by M1, M2, O1, O2 and O3, and ii) pseudo-tetragonal cage located around the center of the unit cell and walled by M2 and O2 with capping O3. The latter cage contains an $M2_4$ rectangle, as indicated by dashed black lines in the figure. The $M2_4$ rectangle consists of two M2 pairs having the shortest M2–M2 distance of ~2.8 Å and the other two pairs having the distance corresponding to the a-length of ~3.6 Å.

Temperature evolution of the chevron angles of the M1–O1–M1 and M2–O3–M2 pillars in the tunnel are shown in **Fig. 12**. All the chevron angles of the pillars in the tunnel belong to either one of the two. These angles decrease monotonically with increasing temperature. This is a typical indicator how the pillars of the tunnel buckle, and the tunnel clearance along the

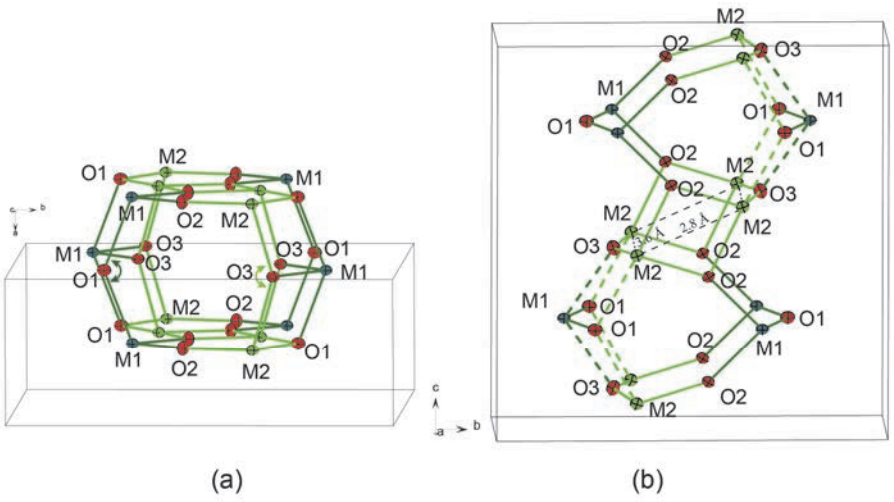

Figure 11. A structural tunnel running in the pseudobrookite-type $M1_1M2_2O_5$ structure, viewed along a direction close to (a) the c-axis and (b) the a-axis. The chevron angles about O1 in the M1–O1–M1 pillar and that about O3 in the M2–O3–M2 pillar are shown by round arrows in (a).

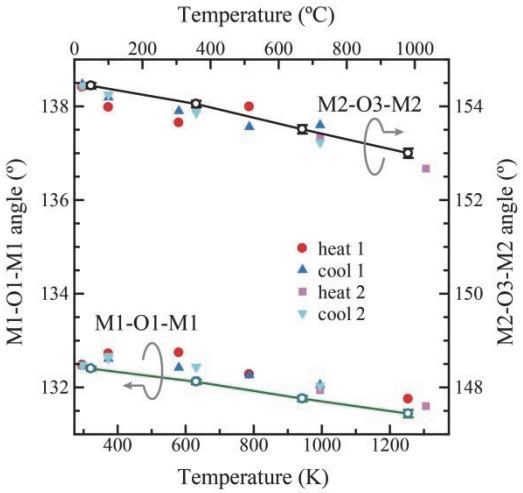

Figure 12. Temperature dependence of the M1–O1–M1 (left-axis) and M2–O3–M2 (right-axis) angles of the chevron-shaped pillars of the tunnel in Al_2TiO_5. The open circles connected by polyline are data obtained from the undoped Al_2TiO_5 during heating. The other scattered marks are those obtained from Mg-doped Al_2TiO_5 during the first heating/cooling and the second heating/cooling processes. The relationship between the colour marks and processes is shown in the legend.

a-axis becomes small during heating. It should be reminded that the M1–O1 and M2–O3 bonds constituting the pillars stay almost unchanged in length (actually, very mildly elongated) during heating (**Fig. 7**).

A schematic illustration of the deformation of tunnel in Al_2TiO_5 at elevated temperatures is shown in **Fig. 13**, where the unit cell dimensions are exaggerated for view purpose in the high-temperature structure while the fractional coordinates and the anisotropic displacement parameters are taken exactly from the data at 1254 K. All the M–O bonds are elongated during heating in order to mitigate the electrostatic repulsion of electron clouds between the nearby atom pairs, in association with the enhanced atomic thermal vibration. As a result, the tunnel expands primarily along the c-axis and secondly along the b-axis by the elongation of the M–O bonds on the ceiling and floor of the tunnel. This tendency is strengthened by the repulsion between the M2 pair on (100), facing each other with the shortest M2–M2 distance of ~2.8 Å in the center cage (**Fig. 11** (b)). The structural evolution takes place minimally under the restriction of the space group symmetry. The larger expansion of the c-length rather than the b-length is of course a result of all-atom displacements, but would be conceivable since the tunnels run in parallel along the c-axis.

When the tunnel expands toward all directions perpendicular to the a-axis, it contracts along their normal, i.e., the a-axis, by the Poisson effect [21]. From the atomistic point of view, the contraction occurs by the pillar buckling; extrusion of atoms at the middle of the chevron-shaped pillars toward outside of the tunnel. From the macroscopic point of view, on the other hand, the phenomenon manifests itself in the contraction of the substance along the a-axis. It should be once recalled that this atomistic deformation occurs compatibly with the elongation of 'all' M–O bond-lengths during heating.

4. Conclusion

Al_2TiO_5 and related compounds are known to show a

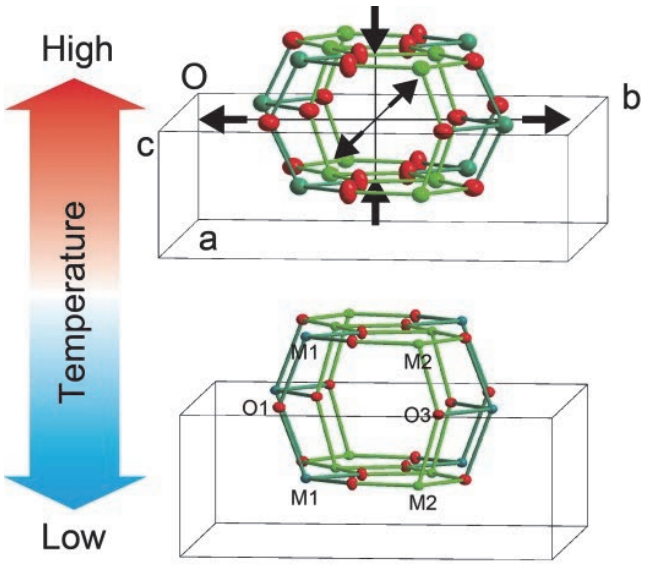

Figure 13. Schematic diagram to show changes in the shape of the tunnel in Al_2TiO_5 with temperature. Deformation directions during heating are shown by black arrows.

large anisotropy in their thermal expansion properties. In the present study, the structural basis for this anisotropy has been explained through the in-situ single-crystal X-ray diffraction experiments carried out in the temperature range up to ~1300 K. The structure contains tunnels running along the c-axis, which change shape gradually with increasing temperature. The change in the shape of tunnel has two features; one is a buckling deformation of the chevron-shaped pillars composed of metal–oxygen bonds in association with the expansion of the tunnel along all directions perpendicular to the a-axis, and the other is the associated Poisson contraction along the a-axis. The former expansion is not isotropic on all directions perpendicular to the a-axis, but anisotropic due to a complexity in atomic arrangement constituting the tunnel. The overall atomistic deformation results in the negative macroscopic mean thermal expansion coefficients of approximately -3.8×10^{-6} along the a-axis, and, in contrast, positive and relatively large values of approximately 11.0×10^{-6} along the b-axis and 20.0×10^{-6} along the c-axis.

The population analysis of the metal atom sites of M1 at 4*c* and M2 at 8*f* in the space group *Cmcm* revealed that the structural formula of the undoped Al_2TiO_5 can be written as

$^{[4c]}[Al_{0.615(3)}Ti_{0.385(3)}]^{[8f]}[Al_{0.693(2)}Ti_{0.307(2)}]_2O_5$,

and that of the Mg-doped one is

$^{[4c]}[Al_{0.616(9)}Ti_{0.384(9)}]^{[8f]}[Al_{0.562(4)}Ti_{0.373(4)}Mg_{0.065(10)}]_2O_5$.

The site preference of metal atoms with different oxidation states and different ionic sizes is rather complicated but can be essentially explained from their adaptability to the geometry of coordination polyhedra around M1 and M2, and the electrostatic repulsion between the M2–M2 pair separated by a very short distance of ~2.8 Å.

A hysteresis in the negative thermal expansion of the a-length was observed for the Mg-doped Al_2TiO_5 sample in the first heating/cooling processes, which was detected neither in the second heating/cooling processes in the same sample nor in the undoped Al_2TiO_5 sample. Considering that a similar hysteresis has been reported in the literature, however, it indicates a presence of concealed phenomenon intrinsic to this substance, while the details are left for future study.

5. Acknowledgement

We are grateful to the staff members, especially Hisashi Hibino, of the Advanced Ceramics Research Center, Nagoya Institute of Technology, for the electron backscattering diffraction and the energy dispersive X-ray spectroscopy analyses.

References

[1] L. Pauling, Z. Kristallogr., 73 (1930) 97.
[2] A.E. Austin, C.M. Schwartz, Acta Crystallographica, 6 (1953) 812-813.
[3] E. Kato, K. Daimon, J. Takahashi, J. Am. Ceram. Soc., 63 (1980) 355-356.
[4] Y. Ohya, Z. Nakagawa, K. Hamano, J. Am. Ceram. Soc., 70 (1987) C-184-C-186.
[5] K. Daimon, J. Ceram. Soc. Jpn., 98 (1990) 365-369.
[6] C. Babelot, A. Guignard, M. Huger, C. Gault, T. Chotard, T. Ota, N. Adachi, Journal of Materials Science, 46 (2011) 1211-1219.
[7] Y. Ohya, S. Yamamoto, T. Ban, M. Tanaka, S. Kitaoka, J. Eur. Ceram. Soc., 37 (2017) 1673-1680.
[8] B. Morosin, R.W. Lynch, Acta Crystallogr. Sect. B, 28 (1972) 1040-1046.
[9] R.D. Skala, D. Li, I.M. Low, J. Eur. Ceram. Soc., 29 (2009) 67-75.
[10] A. Gallet-Doncieux, P. Michaud, M. Huger, T. Chotard, N. Ishizawa, T. Ota, Proceedings of the Unified International Technical Conference on Refractories (UNITECR 2011), Kyoto, (2011) 3211.
[11] Bruker, SAINT and Smart Apex II, Bruker AXS Inc., Madison, Wiskonsin, USA., (2007).
[12] Bruker, SADABS, TWINABS. Bruker AXS Inc., Madison, Wisconsin, USA. (2001).
[13] L. Palatinus, G. Chapuis, J. Appl. Crystallogr., 40 (2007) 786-790.
[14] V. Petříček, M. Dušek, L. Palatinus, Z. Kristallogr., 229 (2014) 345.
[15] K. Brandenburg, H. Putz, Crystal Impact GbR, Postfach 1251, D-53002 Bonn, Germany, Version 4.3 (2016).
[16] K. Momma, F. Izumi, J. Appl. Crystallogr., 44 (2011) 1272-1276.
[17] R.D. Shannon, C.T. Prewitt, Acta Crystallogr., B25 (1969) 925-946.
[18] S.T. Norberg, N. Ishizawa, S. Hoffmann, M. Yoshimura, Acta Crystallogr. Sect. E, 61 (2005) i160-i162.
[19] A.R. Lennie, K.S. Knight, C.M.B. Henderson, Am. Mineral., 92 (2007) 1165-1180.
[20] K. Robinson, G.V. Gibbs, P.H. Ribbe, Science, 172 (1971) 567-570.
[21] S.D. Poisson, Ann. Chim. Phys., 36 (1827) 384-387.